**Across-track Extension of Retrieved Cloud and Aerosol Properties
for the EarthCARE Mission: The ACM-3D Product**

ZHIPENG QU

Environment and Climate Change Canada, Toronto, ON, Canada

HOWARD W. BARKER*

Environment and Climate Change Canada, Victoria, BC, Canada
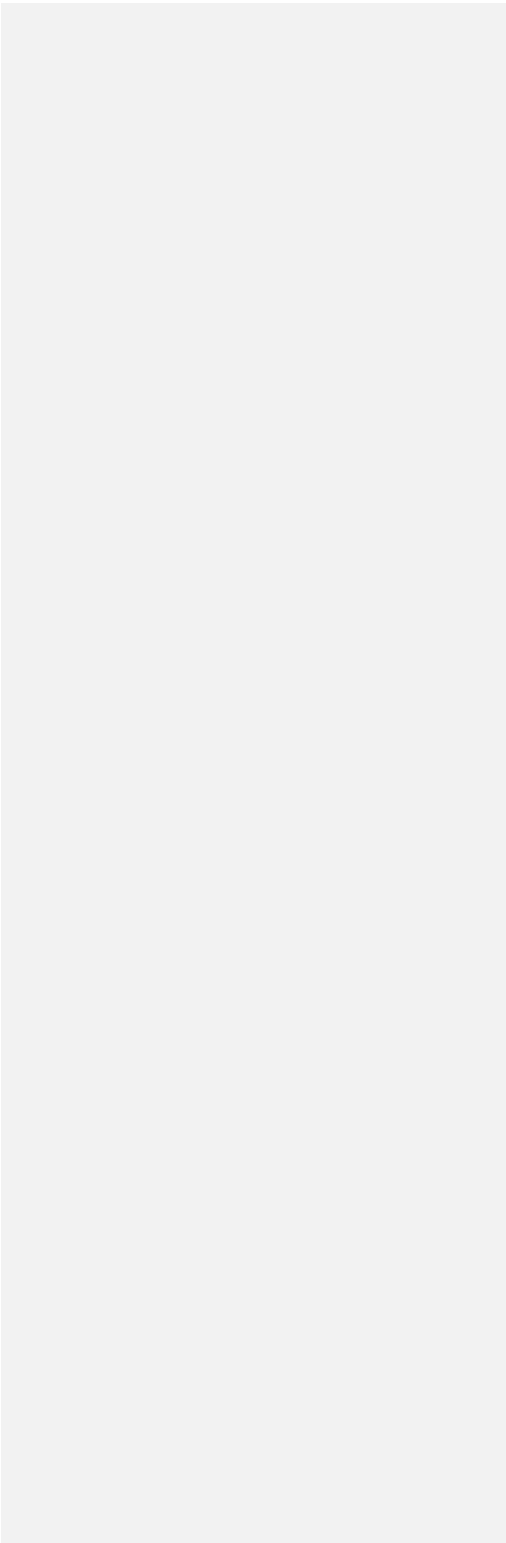
JASON N. S. COLE   MARK W. SHEPHARD

Environment and Climate Change Canada, Toronto, ON, Canada

* *Corresponding author address*: Howard Barker; howard.barker@ec.gc.ca

Abstract

The narrow cross-section of cloud and aerosol properties retrieved by L2-algorithms that operate on data from EarthCARE's nadir-pointing sensors gets "broadened" across-track by an algorithm that is described and demonstrated here. This *Scene Construction Algorithm* (SCA) consists of four components. At its core is a radiance-matching procedure that works with measurements made by EarthCARE's Multi-Spectral Imager (MSI). In essence, an off-nadir pixel gets filled with retrieved profiles that are associated with a (nearby) nadir pixel whose MSI radiances best match those of the off-nadir pixel. The SCA constructs a 3D array of cloud and aerosol (and surface) properties for entire *frames* that measure ~6,000 km along-track by 150 km across-track (i.e., the MSI's full swath). Constructed domains out to ~15 km across-track on both sides of nadir are used explicitly downstream as input for 3D radiative transfer models that predict top-of-atmosphere (TOA) broadband solar and thermal fluxes and radiances. These quantities are compared to commensurate measurements made by EarthCARE's BroadBand Radiometer (BBR), thus facilitating a continuous closure assessment of the retrievals. Three 6,000 km x 200 km frames of synthetic EarthCARE observations were used to demonstrate the SCA. The main conclusion is that errors in modelled TOA fluxes that stem from use of 3D domains produced by the SCA are expected to be less than ± 5 W m^{-2} and rarely larger than ± 10 W m^{-2}. As such, the SCA, as purveyor of information needed to run 3D radiative transfer models, should help more than hinder the radiative closure assessment of EarthCARE's L2 retrievals.

Deleted: sub-algorithms.

1. Introduction

The objective of the EarthCARE satellite mission is to help improve numerical predictions of weather, air quality, and climatic change via application of synergistic L2-retrieval algorithms to observational data from its cloud-profiling radar (CPR), backscattering lidar (ATLID), and passive multi-spectral imager (MSI) (Illingworth et al. 2015). EarthCARE's overarching scientific goal (ESA 2001) is to retrieve cloud and aerosol properties with enough accuracy that when used to initialize atmospheric radiative transfer (RT) models, simulated top-of-atmosphere (TOA) broad-band radiative fluxes, for domains covering ~100 km^2, agree with their observational-based coun-terparts to within ±10 W m^{-2} *more often than not*. "Observed" TOA fluxes derive from radiances measured by EarthCARE's multi-angle broadband radiometer (BBR). As the latter are not used by retrieval algorithms, comparing them to modelled values, obtained by RT models operating on retrieved quantities, affects a "moderately stringent" verification of the retrievals (Barker et al. 2023); "moderately stringent" because BBR radiances consist, in part, of photons that share the same gaseous pathlength and number of cloud-aerosol-surface scattering event distributions as those that constitute MSI radiances. These imperfections aside, this radiative closure verification is a well-defined and cost-effective final stage in EarthCARE's formal processing chain (Eisinger et al. 2023).

In light of EarthCARE's ambitious goal of limiting differences between measured and modelled TOA fluxes to ±10 W m^{-2} when averaged over "assessment domains" that measure ~5 km across-track by ~21 km along-track, the usefulness of its radiative closure programme depends much on reducing errors and uncertainties in: BBR measurements; variables needed by RT models that are not provided by EarthCARE observations; and RT models. Included in this are issues of observa-tional geometry that face use of BBR data for EarthCARE's closure assessment. First, L2-retrieved

Deleted: "production model"

79   profiles are ~1 km in diameter, while the BBR was designed to perform best for footprints of ~10

80   x 10 km. For this configuration, fluxes and radiances computed for sequences of retrieved profiles

81   contribute only ~10% of the signal to each BBR footprint (or pixel). Second, at only ~1 km wide,

82   net horizontal fluxes for each retrieved column, and sequences of them, will rarely be close to zero

83   (e.g., Barker and Li 1997; Marshak et al. 1998). This implies that 3D RT models, as opposed to

84   their ubiquitous 1D counterparts, will be required to make EarthCARE's radiative closure assess-

85   ment fruitful (Illingworth et al. 2015). Hence the need for 3D arrays of data that describe the Earth-

86   atmosphere system adjacent to the ~1 km-wide retrieved L2-cross-section.

87   Fortunately, BBR data are not bound to 10 km resolution, as point-spread function widths of its

88   native radiances are ~0.7 km. This offers much flexibility to the design of the closure assessment

89   (e.g., Tornow et al. 2018). The extreme case is to use a single along-track line of BBR radiances

90   that overlap, at best approximately, the ~1 km wide curtain of L2-retrieved profiles, referred to

91   hereinafter as the L2-plane. This would, however, degrade BBR performance, via reduced signal-

92   to-noise ratio and pointing accuracy, and thus weaken closure assessments. Alternatively, one

93   could attempt an across-track "broadening" of the L2-plane so as to cover as many BBR native

94   radiances as deemed necessary. Regardless of the route taken and the size of domains over which

95   closure assessments are to be performed, there is the ever-present related issue of lateral flow of

96   photons both within assessment domains *and* between assessment domains and their adjacent areas.

97   Taking these issues together, EarthCARE's science team opted for its closure assessment experi-

98   ment to use 3D RT models applied to assessment domains centred on the L2-plane with across-

99   track widths appreciably greater than 1 km (Illingworth et al. 2015).

Deleted: .

The method for approximating 3D geophysical variables adjacent to the L2-plane, in order to safely use both 3D RT models and BBR data, is the radiance-matching *Scene Construction Algorithm* (SCA) (Barker et al. 2011), which forms the basis of the ACM-3D processor. The purpose of the current paper is to recap, in section 2, the SCA, present several operational details associated with it, and demonstrate, in section 3, its overall performance using simulated observations for a virtual Earth-observation system (Qu et al. 2023; Donovan et al. 2023). Application of RT models to SCA products and subsequent radiative closure assessments for the same virtual environments are discussed by Cole et al. (2023) and Barker et al. (2023). A brief discussion is given in section 4.

2. 3D Atmosphere-Surface Scene Construction Algorithm

To begin, EarthCARE's products are partitioned into ~6,565 km long "frames", which makes six frames / orbit. Position in a frame is defined by the Joint Standard Grid (JSG). Each frame contains N_{JSG} L2-retrieved columns along-track. Frame widths are 150 km as defined by the MSI's swath; 35 km to the right and 115 km to the left of the L2-plane (relative to the satellite's direction of motion). Some algorithms require data beyond nadir, and so each frame's files also contain n_{ε} swaths of data from neighbouring frames. JSG coördinates are denoted as (i, j), with i running along-track from $1 - n_{\varepsilon}$ to $N_{JSG} + n_{\varepsilon}$, and j running perpendicular to the L2-plane, which is located at $j = 0$.

As documented by Cole et al. (2023), EarthCARE's radiative products are produced by 1D and 3D broadband RT models. Some of these products are used to perform radiative closure assessments of L2-retrievals (see Barker et al. 2023). While 1D RT models are applied, in ACM-RT (see

124   Cole et al. 2023), to all non-corrupt columns in the L2-plane, their results are averaged over small

125   domains D, in processor ACMB-DF where radiative closure is assessed, referred to hereinafter as

126   *assessment domains*, whose along-track centres, at $j = 0$, are the L2-plane. Conversely, 3D RT

127   models operate directly on D and domain-average results are computed in ACM-RT and used in

128   ACMB-DF. The structure of D for $j \neq 0$ is defined by the 3D *Scene Construction Algorithm*

129   (SCA), which is explained in the following subsections. Along-track lengths of D, in terms of JSG

130   cells, are n_{assess} columns(pixels), while their across-track half-widths are m_{assess}, making full across-

131   track widths $2m_{assess} + 1$ columns(pixels). The initial plan is to fix m_{assess} and n_{assess} at 2 and 21,

132   respectively. Thus, D are $\sim 5 \times 21$ km, so their areal extents, regardless of location, are ~ 100 km^2,

133   which is what the BBR was designed to operate at (see Illingworth et al. 2015).

134   The operational SCA is made up of several sub-algorithms. At its core is definition of D at

135     $(i, j \neq 0)$ via MSI radiance-matching (Barker et al. 2011). Other crucial components include: def-

136   inition of buffer-zones around D, as required by the 3D RT models; screening and ranking of D

137   in an attempt to maximize the usefulness of the radiative closure assessment process; and estima-

138   tion of errors for TOA fluxes and radiances that stem from the radiance-matching algorithm. To

139   improve readability of the main text, many details of these sub-algorithms are presented in Appen-

140   dices. General results are shown and discussed in Section 3.

Deleted: , in ACMB-DF,
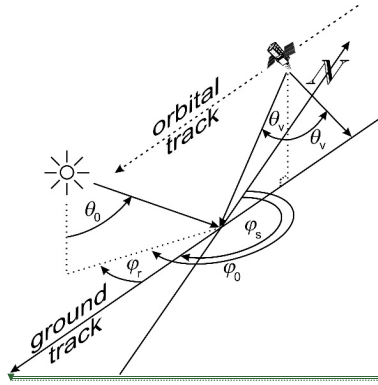
Figure 1: Schematic showing solar zenith angle θ_0, solar azimuth angle relative to north φ_0, satellite-tracking vectors relative to north φ_s, solar azimuth angle relative to satellite-tracking direction φ_r, and the BBR's two off-nadir zenith angles θ_v.
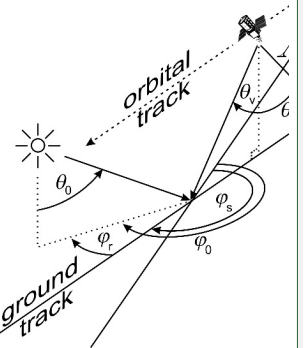
2.1. Radiance matching

The core of the SCA, and thus the ACM-3D processor, is passive narrowband radiance-matching of an off-nadir MSI pixel's spectral radiances with their nadir counterparts along the L2-plane (Barker et al. 2011). As this methodology has been described and used elsewhere (Barker et al. 2011; 2012; 2014; Sun et al. 2016), it is recapped briefly here, with details reiterated in Appendix A. Note that all independent variables referred to here are available to the ACM-3D processor from other EarthCARE processors; all of which are reported on in this special issue.

Let $r_k(i,j)$ be MSI radiances, for the kth channel, where values at position $(i, j=0)$ align along the L2-plane and have geophysical profiles associated with them. When seeking to populate an off-nadir *recipient* column at $(i, j \neq 0)$ with a suitable *donor* from the L2-plane, the algorithm quantifies

165 how well $r_k(i, j \neq 0)$ match $r_k(m, j = 0)$ for all $m \in [i - M, i + M]$; M being the number of JSG

166 pixels, forward and backward, along the L2-plane one is prepared to allow the algorithm to search.

167 While M could depend on a host of variables, a default value of 200 has been used thus far. As

168 explained in Appendix A, for a nadir pixel to be a potential donor, the recipient's and donor's

169 surface types (land, sea, and snow/ice) must match, and cosine of solar zenith angles μ_0 and azi-

170 muth angles between Sun and satellite tracking direction φ_r must differ by less than specified

171 amounts. Figure 1 shows a schematic of solar-satellite geometry. While the recipient and L2-donor

172 pixels could be required to have the same cloud phase, the intention all along has been for the

173 algorithm to rely just on radiances, not other algorithms.

174   Of those L2-plane pixels whose MSI radiances best resemble those at $(i, j \neq 0)$, the one lying

175 physically closest to $(i, j \neq 0)$ becomes the donor, and its profiles of geophysical information get

176 replicated at $(i, j \neq 0)$. This procedure is performed for all $(i, j \neq 0)$ across the MSI's swath; pixels

177 at $(i, 0)$ donate to themselves. The result is *construction* of a 3D atmosphere-surface domain made-

178 up of profiles from the L2-plane. Correspondingly, MSI imagery are *reconstructed*, too. Figure 2

179 shows a schematic of the radiance-matching procedure. Hereinafter, values at (i, j) that are based

180 on the SCA are indexed as $(m*(i, j), 0)$, which ties them back to the $m*(i, j)^{\text{th}}$ column/pixel along
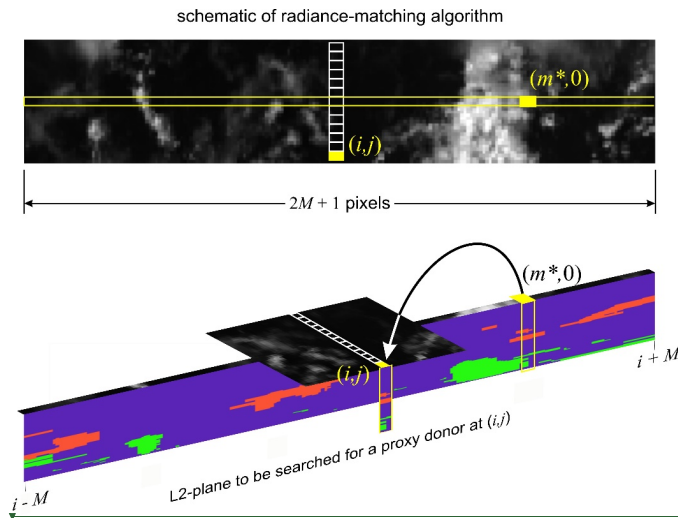
181 the L2-plane.

182
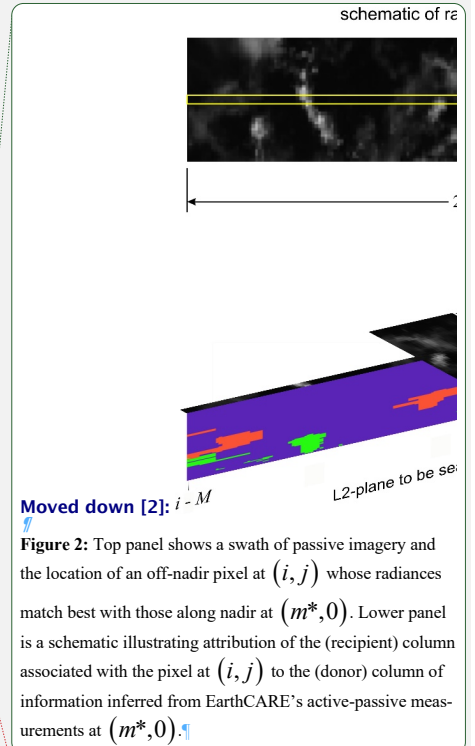
schematic of ra

Moved down [2]: $i - M$

L2-plane to be se

Figure 2: Top panel shows a swath of passive imagery and the location of an off-nadir pixel at (i, j) whose radiances match best with those along nadir at $(m*, 0)$. Lower panel is a schematic illustrating attribution of the (recipient) column associated with the pixel at (i, j) to the (donor) column of information inferred from EarthCARE's active-passive measurements at $(m*, 0)$.

Deleted:

schematic of radiance-matching algorithm

$(m^*,0)$

(i,j)

$2M + 1$ pixels

$(m^*,0)$

$i + M$

(i,j)

L2-plane to be searched for a proxy donor at (i,j)

$i - M$

Figure 2: Top panel shows a swath of passive imagery and the location of an off-nadir pixel at (i,j) whose radiances match best with those along nadir at $(m^*,0)$. Lower panel is a schematic illustrating attribution of the (recipient) column associated with the pixel at (i,j) to the (donor) column of information inferred from EarthCARE's active-passive measurements at $(m^*,0)$.

2.2. Assessment domains and their buffer-zones

The 3D RT models used for EarthCARE employ cyclic horizontal boundary conditions. Real cloudy domains and those produced by the SCA are, however, non-cyclical and so when 3D RT models operate on them, adverse effects near the perimeter of D are affected by photon paths crossing discontinuous optical properties. One way to deal with this is to add atmosphere and surface to all edges of D so as to, not eliminate but rather, displace away from D any adverse effects

216 set-up by the assumed cyclic boundary conditions. Hereinafter, the domain resulting from the com-

217 bination of D and its buffer-zones is denoted as D^+.
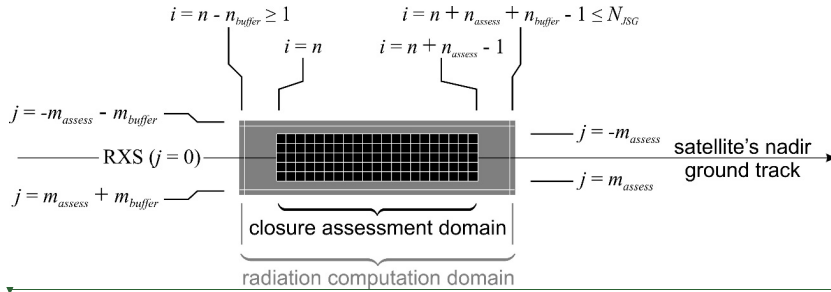
219 **Figure** 3: Schematic showing the radiative closure assessment domain $D(i)$ (black) and the radi-
220 ation computation domain $D^+(i)$; the union of $D(i)$ and the buffer-zone (shaded). See the text
221 for definitions of indices.

223 Buffer-zones also accommodate the fact that the BBR's oblique radiances associated with D

224 consist partly of photons that were scattered by the atmosphere and surface outside of D. Barker

225 et al. (2015) described an adjustment to 3D RT Monte Carlo models that approximates fractional

226 contributions to a BBR radiance from photons whose last scattering event, by any particular scat-

227 tering species, took place in D. Their algorithm, however, is too time-consuming for EarthCARE's

228 official data processing system. Nevertheless, the buffer-zone should adequately capture contribu-
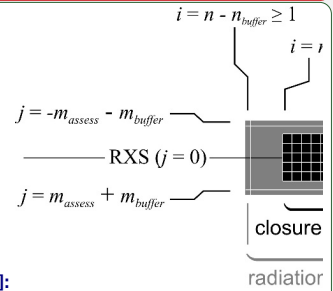
229 tions to BBR radiances that come from beyond D.

230 Setting the along- and across-track dimensions of buffer-zones is described in detail in Appendix

231 B. *Figure 3* shows D, its associated D^+, and the indices that locate them on the JSG. The number

232 of pixels in the along-track that are out in front $n_{buffer}^{\searrow}$ and trailing $n_{buffer}^{\swarrow}$ D can vary and depend on

233 the minimum along-track buffer length $d_{\parallel}^{min}$, assumed to be ~5 km, BBR viewing zenith angle θ_v

242 , and nearby cloudtop altitudes $h\big(m*(i,j),0\big)$ as defined by the radiance-matching algorithm. Fig-

243 ure *4* is a schematic of this process which is detailed in Appendix B.

Moved down [4]: Note that $n_{buffer}^{\swarrow}$ and $n_{buffer}^{\searrow}$ are independent of θ_0.

Deleted: This is because for EarthCARE's orbit; over 80% of observations with $\theta_0 < 90°$ have $30° < \varphi_r < 150°$ implying that, for most cases, projection of direct-beam (and hence cloud shadows) into the along-track walls of D will be small. Exceptions are for very large θ_0 with $\varphi_r < 30°$ or $\varphi_r > 150°$; but these cases are usually avoided because the RT models rely on the plane-parallel approximation.¶

244

Figure 4: Schematic showing the procedure for finding along-track buffer-zone size; in this case $n_{buffer}^{\swarrow}$. (a) $h_D^{\max}$ is maximum cloudtop altitude in assessment domain D, and $d_{\parallel}^{\min}$ is the smallest size buffer-zone allowed. (b) As the algorithm searches out in front of D, a cloud is encountered; part of which lies between D and the satellite, and so the buffer-zone increases. (c) Continuing the search, still a higher cloud is encountered between D and the satellite, thus increasing the buffer-zone further. (d) There is still more cloud between D and the satellite so the buffer-zone increases again, this time to its final value of $n_{buffer}^{\swarrow}$, despite the possibility of cloudtops further out being higher yet still. See text and Appendix B for details.

253

Formatted: Space Before: 6 pt

254 Note that $n_{buffer}^{\swarrow}$ and $n_{buffer}^{\searrow}$ are independent of θ_0. This is because for EarthCARE's orbit, over

Moved (insertion) [4]

255 80% of observations with $\theta_0 < 90°$ have $30° < \varphi_r < 150°$ implying that, for most cases, projection

Field Code Changed

Field Code Changed

266   of direct-beam (and hence cloud shadows) into the along-track walls of D will be small. Excep-

267   tions are for very large θ_0 with $\varphi_r < 30°$ or $\varphi_r > 150°$, but these cases are usually avoided because

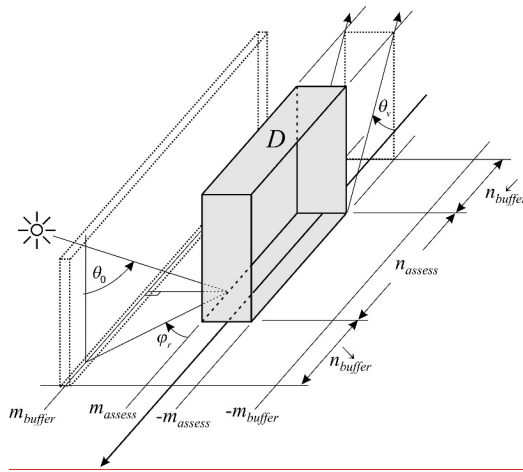268   the RT models rely on the plane-parallel approximation.

269

270   **Figure 5**: Schematic showing the procedure for finding the size of the cross-track buffer-zone
271   size m_{buffer}. See text and Appendix B for details.

272

273   Determination of the size of cross-track buffer-zones m_{buffer} depends on $h\left(m*(i,j),0\right)$ adjacent

274   to the sunlit side of D and minimum size for the across-track buffer-zone $d_{\perp}^{\min}$. If a cloud to the

275   side of D casts a shadow that falls onto the region formed by D and its along-track buffer-zones,

276   then the cross-track buffer-zone extends to include the cloud doing the shadowing. Unlike the

277   along-track, m_{buffer} gets applied to both sides of D. Figure 5 summarizes definition of m_{buffer}.

2.3. Screening radiative closure assessment domains

Due to computational limitations and time constraints on product production, it is anticipated that only a small number of D per frame will participate in the 3D RT radiative closure exercise (i.e., processor ACMB-DF). Hence, D that emerge from the SCA must be "screened and ranked" to ensure that an adequate range of cases, from "simple" to "complex", be assessed in order to: i) provide well-rounded pictures of algorithmic performances; ii) gauge whether mission objectives are being met; and iii) provide guidance to data users who wish to focus on select conditions. At the same time, screening and ranking should be flexible enough to be changed during the mission. For instance, "simple" scenarios are likely to be of particular interest during the commissioning phase (e.g., mono-phase, single-layer, overcast clouds).

The screening process eliminates D that are likely to yield uninformative assessments. It has three stages as described in the following subsections. Each frame has two sets of surviving assessment domains: $\mathrm{D_{1D}}$ contains domains that 1D RT results are averaged over; $\mathrm{D_{3D}}$ contains domains that 3D RT models get applied to. Domains in $\mathrm{D_{1D}}$ and $\mathrm{D_{3D}}$ consist, respectively, of *radiative assessment domains* D and *radiative computation domains* D^+ (see Figure 3).

2.3.1. Screening Stage 1: Failed retrievals and corrupt data

If there are corrupt data or failed retrievals for any column in either D or D^+, the domain will not be forwarded to subsequent processes. This is because they simply cannot be used by 3D RT models. Examples of failed retrievals include algorithms that did not converge to a solution or converged to values that are out of bounds. Corrupt data, on the other hand, includes failure at the L1 level and data corrupted during transmission.
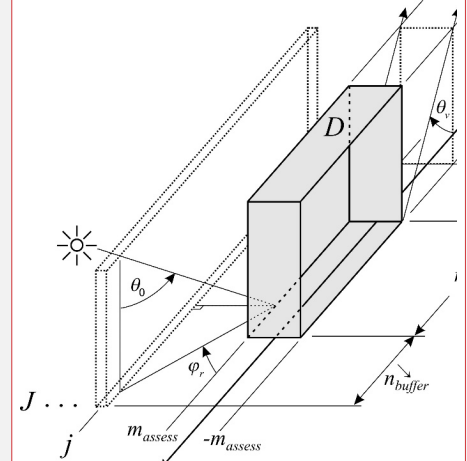
Figure 5: Schematic showing the procedure for finding the size of the cross-track buffer-zone

307   *2.3.2. Screening Stage 2: Geophysical conditions*

308   *a) Solar zenith angle*

309   Generally speaking, solar RT becomes increasingly complicated as solar zenith angle θ_0 increases.

310   This is because: i) radiances and fluxes for EarthCARE-sized domains will depend increasingly on

311   conditions outside D and D^+; and ii) Earth's sphericity becomes increasingly important; Earth-

312   CARE's RT codes are plane-parallel models. Not only do large θ_0 impact the SCA directly, they

313   stress retrieval algorithms that use MSI data. Hence, when the Sun is up, D or D^+ must have

314    $$\max\left\{\theta_0\left(i,j\right)\right\}<\theta_0^* \quad \forall\left(i,j\right)\in D \text{ or } D^+, \tag{1}$$

315   where θ_0^* is the maximum allowed value of θ_0, in order for solar radiances to be considered by the

316   SCA. Initially, $\theta_0^* = 75°$. When the Sun is down, however, data from solar channels are simply not

317   used; as shown by Barker et al. (2011), this diminishes the SCA's performance.

318   *b) Single surface type*

319   To focus closure assessments on retrieved cloud and aerosol properties, and reduce potential com-

320   plications due to boundary conditions that are outside the purview of EarthCARE's retrievals, D

321   and D^+ must have at least 90% of its area occupied by a single broad class of surface type. These

322   types are: water (oceans and lakes), land, and ice.

323   *c) Homogeneous land surfaces*

324   Each JSG pixel has a land-type designation obtained from the International Geosphere–Biosphere

325   Programme (USGS 2018). Let f_ℓ be the fraction of JSG pixels in either D or D^+ that corresponds

329   to the ℓth surface-type. For reasons listed above, if D and D^+ is a "land" domain, then for them to

330   be included in D_{1D} and D_{3D}, they must have

331
$$\max\{f_\ell\} > f^*, \tag{2}$$

332   where f^* is set initially to 0.9.

333   *d) Surface elevation*

334   Uncertainties in spectral bidirectional reflectance and emittance functions as well as albedos and

335   emissivities are complicated by variations in surface elevation. In an attempt to limit uncertainties

336   associated with the setting of these lower boundary conditions in the RT models, only very flat

337   assessment domains are allowed. Hence, if σ_{srf} is standard deviation of surface elevation for D or

338   D^+, then for them to be included in D_{1D} and D_{3D}, they must have

339
$$\sigma_{srf} < \sigma^*_{sfc}, \tag{3}$$

340   where σ^*_{sfc} is set initially to 0.1 km.

341   *2.3.3. Screening Stage 3: Quality of radiance matching*

342   Where SCA reconstructed MSI radiances are poor, it is reasonable to assume that corresponding

343   constructed 3D domains are, too. Thus, the final screening stage addresses the quality of recon-

344   structed MSI imagery, but it also provides bias-correction estimates for modelled TOA quantities.

345   For an assessment domain D of n_{assess} JSG pixels along-track and $j \in [-m_{assess}, m_{assess}]$ across-

346   track, the nth moment of r_k over D, excluding the L2-line along $j = 0$, is

347
$$\left\langle r_k^n \right\rangle = \frac{1}{2m_{assess}n_{assess}} \sum_{i=i_1}^{i_1+n_{assess}-1} \sum_{j\in\left[-m_{assess},-1\right]\cup\left[1,m_{assess}\right]} r_k^n(i,j). \tag{4}$$

348 where i_1 is along-track JSG index at the edge of D. Corresponding reconstructed values are

349
$$\left\langle \hat{r}_k^n \right\rangle = \frac{1}{2m_{assess}n_{assess}} \sum_{i=i_1}^{i_1+n_{assess}-1} \sum_{j\in\left[-m_{assess},-1\right]\cup\left[1,m_{assess}\right]} r_k^n(m*(i,j),0). \tag{5}$$

350 Therefore, errors stemming from the radiance-matching algorithm, for the kth MSI channel, are

351
$$\Delta\left\langle \hat{r}_k^n \right\rangle = \left\langle \hat{r}_k^n \right\rangle - \left\langle r_k^n \right\rangle. \tag{6}$$

352 Let $\left\langle F_{\text{SW}} \right\rangle$ and $\left\langle F_{\text{LW}} \right\rangle$ be TOA shortwave (SW) and longwave (LW) fluxes, averaged over D,

353 as estimated by angular direction models in the BMA-FLX processor (Velázquez-Blázquez et al.

354 2023). Since MSI radiances r_1 (0.67 μm) and r_6 (10.80 μm) often correlate well with $\left\langle F_{\text{SW}} \right\rangle$

355 and $\left\langle F_{\text{LW}} \right\rangle$ (Barker et al. 2014), TOA flux bias errors due to the radiance-matching algorithm can

356 be approximated as

357
$$\Delta\left\langle \hat{F}_{\text{SW}} \right\rangle \approx \left\langle F_{\text{SW}} \right\rangle \frac{\left\langle r_1 \right\rangle - \left\langle \hat{r}_1 \right\rangle}{\left\langle \hat{r}_1 \right\rangle} \quad \text{and} \quad \Delta\left\langle \hat{F}_{\text{LW}} \right\rangle \approx \left\langle F_{\text{LW}} \right\rangle \frac{\left\langle r_6 \right\rangle - \left\langle \hat{r}_6 \right\rangle}{\left\langle \hat{r}_6 \right\rangle}. \tag{7}$$

358 If these values satisfy

359
$$\left| \Delta\left\langle \hat{F}_{\text{SW}} \right\rangle \right| > \Delta F_{\text{SW}}^* \mu_0 \quad \text{and} \quad \left| \Delta\left\langle \hat{F}_{\text{LW}} \right\rangle \right| > \Delta F_{\text{LW}}^*, \tag{8}$$

360 where ΔF_{SW}^* and ΔF_{LW}^* are tolerable broadband TOA flux errors arising from the radiance-match-

361 ing algorithm, D is *not* included in neither $\mathbf{D}_{\text{1D}}$ nor $\mathbf{D}_{\text{3D}}$. Both $\Delta\left\langle \hat{F}_{\text{SW}} \right\rangle$ and $\Delta\left\langle \hat{F}_{\text{LW}} \right\rangle$ get passed to

362 ACMB-DF and used to bias-correct estimated TOA fluxes made by both 1D and 3D RT models.

366 This completes the screening processes leaving D_{1D} and D_{3D} with m_{1D} and m_{3D} assessment do-

367 mains, respectively.

368 *Table 1* provides a glimpse into success rates of D and D^+, in all three frames, for the screenings

369 just described using conditions as summarized in the table. Of course, overall success rate for

370 $\theta_0 < 75°$ will be much smaller than most reported here owing to these being "descending" frames.

371 Note also the tendency for success rates for D^+ to be less than those for D. This is because the areal

372 extents of D^+ are always larger than that for D.

373 **Table 1.** Success rates of D and D^+ for the three frames that meet the conditions as listed.

screening variable	condition	Halifax		Baja		Hawaii	
		D	D^+	D	D^+	D	D^+
cloud retrieval quality	more than 10% of columns have valid retrievals	97	98	96	97	97	99
flux reconstruction	both $\Delta F_{SW}^* \mu_0$ and $\Delta F_{LW}^* =$ 5 W m^{-2} (see (8))	100	94	100	93	100	82
solar zenith angle	$\theta_0 < 75°$ *or* $\theta_0 > 90°$	63	59	100	100	100	100
land-sea/water	single type of land/water for at least 90% of a domain	90	90	84	80	100	100
surface type*	surface type for at least 90% of a domain; sunglint occurs for at most 20% of a domain	94	92	84	81	52	49
land surface elevation	standard deviation < 100 m	95	97	79	70	100	100

374

2.4. Ranking radiative assessment domains

376 As noted above, the EarthCARE mission will provide near-real time products with limited compu-

377 tational resources. The portion of the processing chain constrained most by this involves 3D SW

378   RT models. For them to achieve adequate signal-to-noise ratios, just a small fraction of the thou-

379   sands of potential D^+ per frame can be assessed. Thus, to enhance efficacy of the radiative assess-

380   ment process, an algorithm was developed that ranks D^+ in $\mathsf{D_{3D}}$. At any time, ranking can be

381   overruled manually, such as when testing during commissioning phase. The ranking algorithm that

382   was decided upon samples cloud scenarios in proportion to relative frequencies of occurrence.

383   For the initial version of the algorithm, 1 km resolution MODIS-retrieved values (MYD06_L2)

384   of cloud optical depth τ_{cld} and cloudtop pressure p_{cld}, inferred from measurements made during

| | Deleted: for |

385   2020, were grouped into 5 x 21 km arrays, to match EarthCARE's planned 5 x 21 km domains D,

| | Deleted: where |

386   and for each array, mean values $\langle\tau_{cld}\rangle$ and $\langle p_{cld}\rangle$ were computed along with total cloud fraction

387   A_c (Platnick et al. 2015). They were then assigned to bins defined by $10°$ ranges of latitude and

388   longitude, and ranges for $\langle\tau_{cld}\rangle$, $\langle p_{cld}\rangle$, A_c, and time of observation of

389
$$\begin{array}{rl}
\langle\tau_{cld}\rangle & : \quad (0,4];(4,23];(23,150] \\
\langle p_{cld}\rangle & : \quad (0,440];(440,680];(680,\infty) \\
A_c & : \quad (0,0.25];(0.25,0.75];(0.75,0.99];(0.99,1] \\
time & : \quad DJF;MAM;JJA;SON
\end{array} \qquad (9)$$

390   Since only cloud-bearing domains need be ranked, the number of applicable bins is 23,328, of

391   which the nth has N_n domains. When $\theta_0 \geq 90°$, $\langle\tau_{cld}\rangle$ is not retrieved, so the same ranking proce-

392   dure uses the remaining three variables only. Radiative closure assessments for SW fluxes are not

393   done when $75° < \theta_0 < 90°$ on account of too many overwhelming uncertainties with retrievals and

394   plane-parallel RT modelling. Thus, domains in this range are not ranked.

395   For EarthCARE frames with 6,400 1-km L2 columns in the L2-plane there is the potential for

396   6,400 - 21 + 1 = 6,380 (over-sampled) assessment domains, each of which falls into one of the

399 MODIS bins. Now, using only domains with $A_c > 0.01$, form the frame-specific cumulative fre-

400 quency such that the ith domain has a value

$$\mathsf{N}(i) = \frac{1}{\mathsf{N}(6,380)} \sum_{j=1}^{i} N_n(j) \quad ; \quad i = 1,\ldots,N_{cld} \leq 6,380. \tag{10}$$

402 Then, generate a uniform pseudo-random number $\mathsf{R} \in (0,1]$ and find the closest $\mathsf{N}(i)$; this iden-

403 tifies the top-ranked D^+. This is repeated, without replacement, until (possibly all) the domains are

404 ranked. The resulting lists are passed on to ACM-RT.

405 ## 3. Results

406 The SCA's sub-algorithms are discussed in series in this section. The only part not evaluated here

407 is the ranking algorithm (see section 2.4). Its performance is demonstrated in Cole et al. (2023; in

408 this issue) where radiative transfer models act on the highest ranked assessment domains.

409 ### 3.1. Reconstruction of passive radiances

410 Radiance matching is the essence of the SCA, and a sampling of results is provided here. More

411 details are in Barker et al. (2011; 2012; 2014) and Sun et al. (2016). All results presented here, and

412 when $\theta_0 < 90°$, come from using MSI channels: 1 (0.67 μm), 4 (2.21 μm), 5 (8.80 μm), and 7

413 (12.00 μm); i.e., $K_s = 4$ in (11). Obviously, when $\theta_0 \geq 75°$ the SW channels are not used. The

414 largest impediment facing this algorithm is when conditions off the ground-track (GT) differ much

415 from the relatively few samples along the GT (Barker et al. 2011). Figure *6* shows a full-width

416 segment of the *Hawaii* frame that contains both catastrophic failure due to inadequate conditions

417 along the GT and excellent performance for the opposite reason. Approximately 50 - 100 km east

418 of the GT, between 9.5°N and 13°N, radiances, especially channel 1's, that are associated with

419 much cloud are severely short-changed on account of a long stretch of near-cloudless conditions at

420 nadir. To partially remedy this, the algorithm would have to be permitted to search the GT much

421 further than 200 km, as in this example, but in so doing it would run the risk of identifying donor

422 columns associated with increasingly different meteorological conditions. On the other hand, be-

423 tween 5°N and 8°N performance is extremely good across the entire 150 km wide frame.
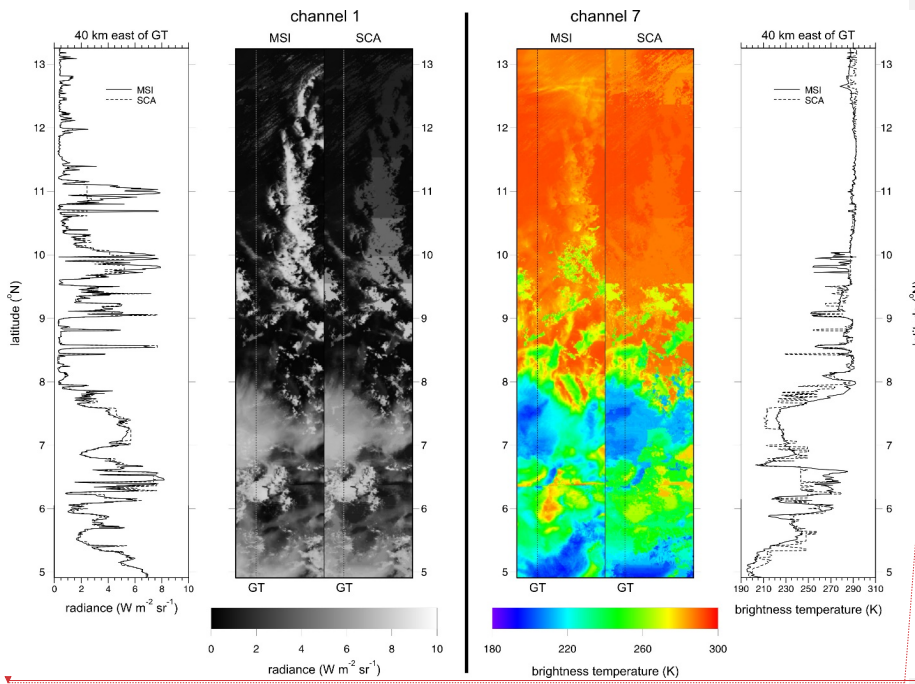
424

425 **Figure 6:** Left panel shows MSI and corresponding SCA channel 1 radiances for a segment of
426 the *Hawaii* frame measuring 150 km wide and 900 km long. Right panel is corresponding bright-
427 ness temperatures from channel 7 radiances. Dashed lines marked GT indicate the ground-track
428 at nadir, which coincides with the L2-plane. Line graphs show MSI and SCA values along the
429 centres of the domains, which are 40 km east of GT.
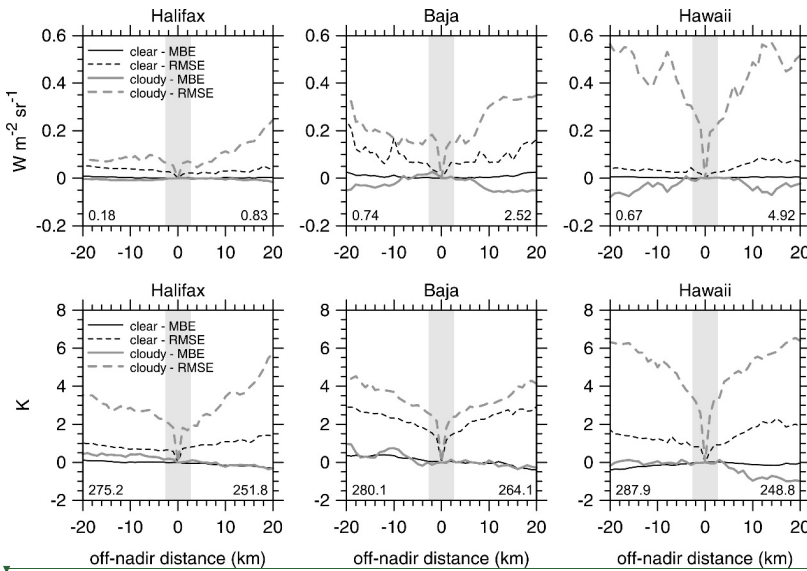
430
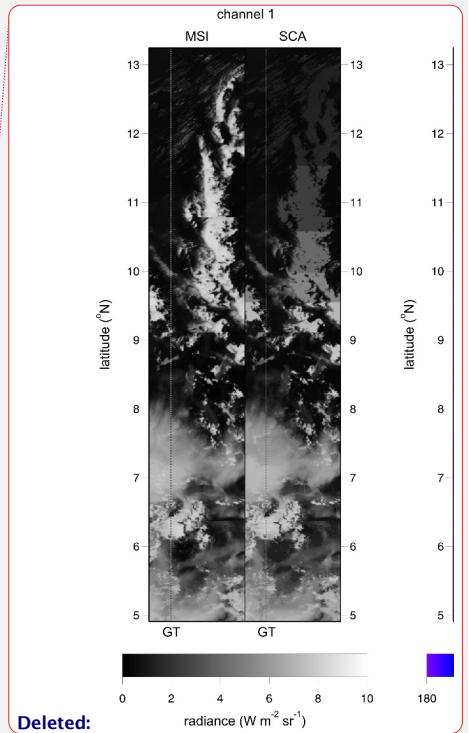
Deleted:

Deleted: 4

Figure 7: Full-frame mean bias errors (MBE) and root mean square errors (RMSE) for SCA reconstructed radiances as functions of distance (-ve values are W) from the ground-track (GT in *Figure 6*). Upper and lower rows are for MSI channel 1 radiances and 7 brightness temperatures. Full-frame mean values are listed on the base of each plot: clear-sky on the left, cloudy-sky on the right. Grey bands indicate EarthCARE's default assessment domains.

Figure 7 shows mean bias errors (MBE) and root mean square errors (RMSE) for reconstructed MSI channels 1 and 7 as functions of distance, east and west, of GT for the full lengths of the three test frames (see Qu et al. 2023). By definition, MBE and RMSE along GT are zero. For channel 1's reconstructions, MBEs out to ±20 km are generally smaller than 0.05 W m^{-2} sr^{-1}, with smaller errors for cloudless pixels. The negative biases for *Baja* and *Hawaii* frames out past ~ 5 km from GT stem from clouds along the GT being slightly darker than those elsewhere over the frames (see Figure 6). Likewise, MBEs for channel 7 are generally smaller than 0.5 K. Over the 5 km wide

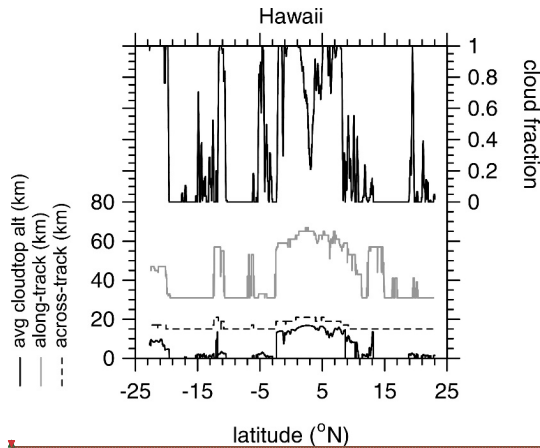449 assessment domains centred on GT, MBEs for both channels are almost negligible relative to the

450 frame-wide average values that are listed along the base of each plot.

451

Figure 8: Along-track and across-track length of assessment domain plus buffer-zones as func-
tions of latitude for the *Hawaii* frame. All assessment domains are 5 km across-track by 21 km
along-track. Minimum size for all buffer-zones is 5 km. Also shown are corresponding values of
mean cloudtop altitude and cloud fraction for 5 x 21 km assessment domains.

456

457 Unlike MBEs, however, RMSE values jump immediately off the GT. In general, they continue

458 to increase with distance from GT, but it is difficult to say at what distance they become unusable.

459 It is important to note that RMSE values plotted here get reduced by at least a factor of 10 for

460 averages over assessment domains.

461 **3.2. Definition of assessment domain buffer-zones**

462 The planned initial default values for both $d_\parallel^{min}$ and $d_\perp^{min}$ is 5 km. Thus, for D measuring 5 x 21

463 km, 3D RT will be applied to D^+ that measure at least ~15 km across-track by ~31 km along-track.

464 Figure *8* shows sizes of D^+ along the *Hawaii* frame. The most notable feature is that along-track
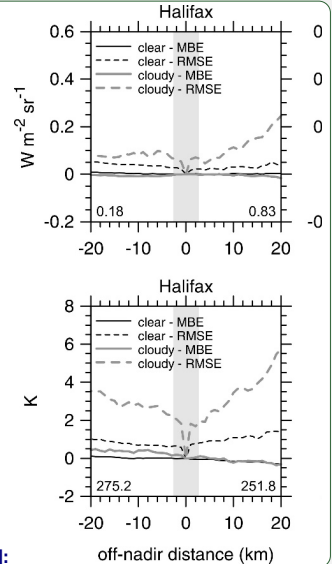
Moved up [6]:

Moved up [7]: Full-frame mean values are listed on the base of each plot: clear-sky on the left, cloudy-sky on the right. Grey bands indicate EarthCARE's default assessment domains.¶

¶   ... [2]

Deleted: ... [1]

Deleted: when for averages over assessment domains. ¶

Formatted: Font: Not Bold

Moved (insertion) [8]

507   lengths vary much more than across-track lengths. This is driven by the fixed along-track off-nadir

508   views of the BBR; whenever cloud occurs, especially high cloud, values of $n_{buffer}^{\searrow}$ and $n_{buffer}^{\swarrow}$ exceed

509   0. Lengths of D^+ maximize between about $3°\,N$ and $6°\,N$ where mean cloudtop altitudes h reach

510   ~17 km; this despite cloud fractions for D^+ being substantially less than 1.

511   While across-track buffer sizes m_{buffer} depend on h, too, they also depend on φ_r and θ_0. Near

512   latitude $10°\,N$, while $\varphi_r \approx 107°$(Sun is shining in almost perpendicular to GT), $\theta_0 \approx 30°$ and so

513   lengths of cloud shadows cast perpendicular to GT are small. As such, there is little need to expand

514   the domain across-track, and so $m_{buffer} = 0$ and cross-track size of D^+ equal the default 15 km.

515   Near latitude $21°\,S$, however, where mean h are the same as near $10°\,N$, clouds are more overcast,

516   but equally important, $\varphi_r \approx 130°$, which is still not far off shining in perpendicular to GT, and

517    $\theta_0 \approx 50°$. Together these conspire to cast cloud shadows well beyond D resulting in D^+ that are

518   slightly larger than the default.

519   **3.3. Estimation of SCA-related bias errors for TOA broadband fluxes**

520   In a manner similar to cloud radiative effects, estimation of errors for TOA broadband radiative

521   fluxes that arise from the SCA process provide a simple, integrated indication of SCA performance.

522   Figure 9 shows cumulative frequency distributions of $\Delta\left\langle \hat{F}_{SW} \right\rangle$ and $\Delta\left\langle \hat{F}_{LW} \right\rangle$ (see (7)), for the *Ha-*

523   *waii* frame. Errors for this frame are the largest of the three. As is often the case, errors tend to be

524   largest for SW fluxes, and increase slightly as assessment domain A_c increases. The latter point

525   basically indicates that the SCA does extremely well in clear-sky conditions; even for the *Baja*

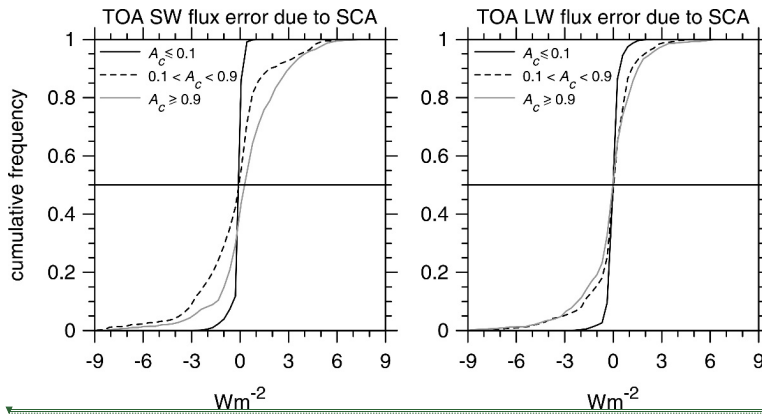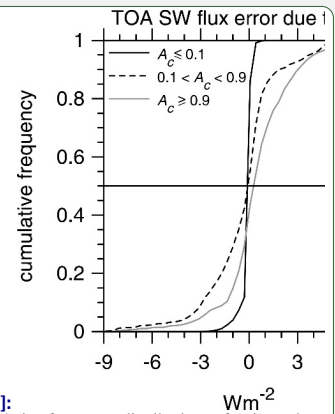526   frame that was mostly over variable land.

527

Figure 9: Cumulative frequency distributions of estimated errors in broadband TOA upwelling
SW and LW fluxes stemming from the SCA for all 5 x 21 km assessment domains in the *Hawaii*
frame. Distributions are partitioned for three ranges of assessment domain total cloud fraction A_c.

531

It is encouraging to see that median errors for both bands are negligible for all conditions. More-

over, as Figure 9 shows, with ~90% of errors being within ±3 W m^{-2}, and slightly better for the

other frames, errors imparted on TOA flux estimates by the SCA will not hinder assessment of

EarthCARE's objective of retrieving cloud-aerosol properties well enough as to be able to model,

on average, TOA fluxes to within ±10 W m^{-2}.

4. Summary and discussion

The EarthCARE satellite mission has set itself a very high bar with its plan to infer cloud and

aerosol properties, from its observations, well enough that when used to initialize radiative transfer

(RT) models, their estimates of TOA fluxes will differ from observed values by, typically, less than

±10 W m^{-2}. To realize, and gauge the success of, this *radiative closure assessment* it will be nec-

essary to employ, operationally, 3D atmospheric RT models. This by itself will set EarthCARE

apart from its predecessors, which have relied entirely on 1D RT models. The immediate issue

Deleted:

552 facing this plan is that L2-retrievals at nadir are just ~1 km wide, and at this scale net fluxes of

553 lateral flowing radiation, not accounted for by 1D RT models, can be substantial (e.g., Marshak et

554 al. 1998). To justifiably use 3D RT models, however, the atmosphere-surface system has to be

555 defined on both sides of the narrow L2-plane. The point of this paper was to demonstrate Earth-

556 CARE's method of expanding its L2-retrievals perpendicular to the L2-plane. At the core of this

557 *3D scene construction algorithm* (SCA) is a radiance-matching (RM) scheme that uses Earth-

558 CARE's MSI passive imagery (cf. Barker et al. 2011; 2012; 2014). There are, however, other as-

559 pects of this process that have been documented here for the first time.

560 Synthetic radiances measured virtually by EarthCARE's MSI for three test frames, which were

561 produced for *end-to-end simulation* of EarthCARE's measurement-processing chain (see Qu et al.

562 2023), were used here to demonstrate the performance of the SCA. "Reconstruction" of measured

563 MSI radiances forms the foundation of the SCA. Basically, off-nadir pixels are paired with a nadir

564 pixel whose spectral radiances best match theirs. The 3D domains to be used by the 3D RT models

565 are "constructed" by taking columns of geophysical information associated with matching nadir

566 pixels and inserting them at the off-nadir pixels.

567 Comparing reconstructed radiances to their observed counterparts provides a straightforward

568 indication of the success of the SCA. If observed radiances are reconstructed poorly, one has to

569 also assume that correspondingly constructed 3D surface-atmosphere domains are unfit for both

570 3D RT models and radiative closure assessment. SCA errors flare-up when conditions needed at

571 off-nadir locations are lacking from the nearby the L2-plane. Typical performances of the SCA

572 were shown in Section 3.1, and as expected, generally erode the further recipient pixels are from

573 their donors. This is not much of an issue for radiative assessment domains themselves, for they

574 extend just 2 km from the L2-plane. Their buffer-zones, however, which were described in section

575 2.2, can be as much as 10 km from the L2-plane (see Figure 3). The reason why assessment do-

576 mains are so small is because EarthCARE's radiative closure assessment seeks to verify the narrow

577 L2 retrievals, not the SCA; the SCA should help achieve this as invisibly as possible.

578 Once defined, assessment domains and their buffer-zones get screened (see section 2.3) in an

579 attempt to identify those most likely to realize useful closure assessments. Furthermore, the inter-

580 section of EarthCARE's data processing limitations with the computational demand of the 3D solar

581 RT model (Cole et al. 2023) forces the need to rank assessment domains to ensure that the few that

582 get assessed per frame lead to good samplings, over the mission's life, of conditions that occur over

583 the globe and the year. This process was described in section 2.4.

584 The simple method of estimating TOA flux bias errors that are likely to arise from the SCA

585 (Barker et al. 2014) was assessed using test frame synthetic observations. Reassuringly, it was

586 shown in Section 3.3 that most TOA flux errors due to the SCA's imperfect atmospheres, for as-

587 sessment domains measuring 5 x 21 km, can be expected to be much smaller, and rarely larger,

588 than EarthCARE's stated goal of ± 10 W m^{-2}.

589 To conclude, it is tempting to view the SCA as a very cost-effective (i.e., almost free) *scanning*

590 *active sensor system* (cf. Illingworth et al. 2018). But one almost always gets what one pays for,

591 and the SCA is, when pushed, no exception. Its performance, especially well-removed from the

592 L2-plane, cannot be expected to rival that of an authentic scanning active sensor system (Barker et

593 al. 2021); to use it as a full-up replacement would be cavalier. In its current role, however, as

594 purveyor of approximate, ancillary information that both facilitates use of 3D RT models and

595 strengthens verification of L2 retrievals, it appears as though its shortcomings will be tolerable and

596 outweighed by its benefits.

597 **Acknowledgements**

Data availability

Data used in this report, and in other EarthCARE reports in this issue, can be obtained at van Zadelhoff et al. (2022).

Deleted: In the short-term, data used for this study can be obtained from the corresponding author. By the time of publication, ECCC will have an official data repository from which data used here will be downloadable.

622 <center>APPENDIX A</center>

623 <center>**Radiance-matching algorithm**</center>

624 Let $r_k(i,j)$ be MSI radiance, for the kth MSI channel, at (i,j) on the joint standard grid (JSG) in which

625 $j = 0$ is along the L2-plane. Following Barker et al. (2011), when seeking to populate a column at

626 $(i, j \neq 0)$ with a suitable proxy from $(i, j = 0)$, begin by computing, for K_s channels,

627
$$F(i,j;m) = \Lambda(i,j;m) \sum_{k=1}^{K_s} a_k \left[\frac{r_k(i,j) - r_k(m,0)}{\max\left[r_k(i,j), r_k(m,0)\right]} \right]^2 \quad ; \quad m \in [i-M, i+M]; j \notin 0, \quad (11)$$

> Deleted: →
> $$F(i,j;m) = \sum_{k=1}^{K_s} a_k \Lambda(i,j;m) \left[\frac{r_k(i,j) - r_k(m,}{\max\left[r_k(i,j), r_k(n} \right.}$$
> Field Code Changed

628 where $(m,0)$ holds potential *donor* profiles for the *recipient* at $(i, j \neq 0)$, a_k are weights that could

629 depend on channel but were assumed to equal 1, and M is number of pixels, forward and backward,

630 along the L2-plane to be searched for a donor. The function $\Lambda(i,j;m)$ is defined as

631
$$\Lambda(i,j;m) = \begin{cases} -1 & ; \quad \chi = .false. \\ 1 & ; \quad \chi = .true. \end{cases} \quad (12)$$

> Deleted: → $\Lambda(i,j;m) = \begin{cases} 0 & ; \quad \chi = .false. \\ 1 & ; \quad \chi = .true. \end{cases}$
> Field Code Changed

632 By requiring

633
$$\chi = \begin{cases} \text{surface at } (i,j) = \text{surface at } (m,0) \\ \quad .and. \\ \left| \mu_0(i,j) - \mu_0(m,0) \right| < \Delta\mu_0 \\ \quad .and. \\ \mu_0(i,j) \cdot \mu_0(m,0) > 0 \\ \quad .and. \\ \left| \varphi_r(i,j) - \varphi_r(m,0) \right| < \Delta\varphi_r \\ \quad .and. \\ m \in [1, N_{JSG}], \end{cases} \quad (13)$$

637   it controls whether or not a pixel at $(m,0)$ is to be considered as a potential donor (see section 2.3).

638   The upper condition means that surface types (land, sea, and snow/ice) must be the same at (i,j)

639   and $(m,0)$. The next two conditions mean that at (i,j) and $(m,0)$ cosine of solar zenith angles

640   μ_0 must differ by less than $\Delta\mu_0 = 0.005$, and the Sun must be up or down at both locations. Next,

641   the difference between solar azimuth angles relative to the satellite's tracking direction φ_r must be

642   less than $\Delta\varphi_r = 5°$. The final condition simply means that the search cannot go past the ends of a

643   frame. It almost goes without saying, but when the Sun is down at $(m,0)$, SW radiances are simply

644   not used in (11).

645   For the $1 \leq M' \leq 2M + 1$ values of $F(i,j;m) \geq 0$ that get computed, define Euclidean distances

646   between the centres of (i,j) and $(m,0)$ as

647
$$L(i,j;m) = \Delta L \left[(i-m)^2 + j^2 \right]^{1/2}, \tag{14}$$

648   where ΔL is horizontal resolution, which for EarthCARE is ~1 km, and sort $F(i,j;m)$ from small-

649   est to largest (i.e., best to worst radiance match), with $L(i,j;m)$ going along passively. Denote the

650   reordered sequences as $\left\{ \hat{F}(i,j;m) \right\}_{m=1}^{M'}$ and $\left\{ \hat{L}(i,j;m) \right\}_{m=1}^{M'}$. Finally, the donor for location $(i, j \neq 0)$

651   is deemed to reside at

652
$$m^*(i,j) = \operatorname*{arg\,min}_{m \in [1, M' \cdot f]} \left\{ \hat{L}(i,j;m) \right\} \tag{15}$$

654 which reads: find m that corresponds to the smallest distance between the recipient at (i,j) and those

655 pixels that constitute the smallest $100f\%$ of $\hat{F}(i,j;m)$. The tuneable parameter f will be set initially to

656 0.05, but this could change (see Barker et al 2011). The procedure outlined here is performed for all

657 $(i,j\neq0)$ across the MSI's swath, with pixels at $(i,0)$ donating to themselves.

658

659　　　　　　　　　　　　　　　　　APPENDIX B

660　　　　　　　　　　　　　**Calculation of buffer-zone sizes**

661　　*a. Along-track length*

662　　Let $h\left(i*(i,j),0\right)$ be cloudtop altitude at JSG cell (i,j) using the SCA's field. Using these values,

663　　define for each i in a frame the highest cloudtop in across-track swaths of JSG pixels spanning the

664　　assessment domains as

665
$$h_{\perp}^{\max}(i) = \max\left\{h\left(i*(i,j),0\right)\right\}: j \in \left[-m_{assess}, m_{assess}\right]. \qquad (16)$$

666　　The symbols $\perp$ and $\|$ indicate across- and along-tracks, respectively. Thus, maximum cloudtop

667　　altitude in an assessment domain $D(n)$ is

668
$$h_{D}^{\max}(n) = \max\left\{h_{\perp}^{\max}(i)\right\}: i \in \left[n, n+n_{assess}-1\right]. \qquad (17)$$

669　　　Consider first the buffer-zone out in front of $D(n)$; applicable most to the BBR's backward

670　　view. The minimum number of JSG pixels that one need be concerned about searching to see if

671　　clouds outside of $D(n)$ obscure part of $D(n)$ is

672
$$n_{buffer} = nint\left(\frac{\max\left\{d_{\|}^{\min}, h_{D}^{\max}(n)\tan\theta_{v}\right\}}{\langle\Delta x\rangle}\right), \qquad (18)$$

673　　where $d_{\|}^{\min}$ is the absolute minimum along-track buffer length, assumed for EarthCARE to be ~5

674　　km, θ_{v} is BBR viewing zenith angle, and $\langle\Delta x\rangle$ is mean length of JSG pixels in the along-track

675   direction. For EarthCARE, $\langle \Delta x \rangle \approx 1$ km. If maximum cloudtop altitude across the entire useable

676   part of the 6,000 km frame is

677

$$h_F^{\max} = \max\left\{h(i,j)\right\} : i \in \left[m_1 + 1, N_{JSG} - m_2 + 1\right], \, j \in \left[-m_{assess}, m_{assess}\right], \qquad (19)$$

678   then the absolute maximum number of JSG pixels one need search for outside of $D(n)$ that might

679   obscure part of $D(n)$ is

680

$$n_{buffer}^{\max} \approx nint\left(\frac{h_F^{\max}\tan\theta_v}{\langle \Delta x \rangle}\right). \qquad (20)$$

681   This can be reduced by knowing the location of the along-track JSG pixel that houses the highest

682   cloud between the last pixel of $D(n)$ and $n_{buffer}^{\max}$ pixels out in front of it. This is expressed as

683

$$n_{buffer}^{\max}(n) = \underset{i \in \left[n + n_{assess} + n_{buffer}(n),\, n + n_{assess} + n_{buffer}(n) + n_{buffer}^{\max}\right]}{\arg\max}\, h_{\perp}^{\max}(i). \qquad (21)$$

684   Proceed then to search

685

$$h_{\perp}^{\max}(i) \ge \frac{\left[i - \left(n + n_{assess}\right)\right]\langle \Delta x \rangle}{\tan\theta_v} : \, i = n + n_{assess} + n_{buffer}, \ldots, n + n_{assess} + n_{buffer}^{\max}(n), \qquad (22)$$

686   where n_{buffer} comes from (18). Let values of i for which the condition in (22) is met form the set

687    $\{i'\}$. Therefore, the size of the buffer-zone for the back-looking view associated with $D(n)$ is

688

$$n_{buffer}^{\swarrow}(n) = \begin{cases} n_{buffer} & ; \quad \text{if (22) is never met} \\ \max\{i'\} & ; \quad \text{if (22) is met.} \end{cases} \qquad (23)$$

689   To set the size of the buffer-zone for the fore-looking view $n_{buffer}^{\searrow}(n)$, (21) through (23) are reap-

690   plied reversing indices. Figure *4* is a schematic of this process.

691   Note that determination of $n_{buffer}^{\swarrow}(n)$ and $n_{buffer}^{\searrow}(n)$ are independent of θ_0. This is because for

692   EarthCARE's orbit over 80% of observations with $\theta_0 < 90°$ have $30° < \varphi_r < 150°$ implying that,

693   for most cases, projection of direct-beam (and hence cloud shadows) into the along-track ends of

694     $D(n)$ will be small. The exceptions are for very large θ_0 with $150° < \varphi_r < 30°$; but most of these

695   cases will be avoided via the screening process as discussed in section 2.3.2.

696   *b. Across-track length*

697   Next, determine the size of across-track buffer-zones m_{buffer}. They are set using cloud information

698   on the sunlit side of $D(n)$. Here the idea is that if a cloud anywhere to the side of D casts a shadow

699   that falls onto the region formed by D and its along-track buffer-zones, then the across-track buffer-

700   zone extends to include the cloud doing the shadowing. Once m_{buffer} is established, it is applied to

701   the opposing side of $D(n)$, too.

702   Begin by setting a minimum size for the buffer-zone of $d_{\perp}^{\min}$, so that searching starts at cross-

703   track JSG pixel $\pm m_{assess} \pm m_{buffer}$, where $m_{buffer} = nint\left(d_{\perp}^{\min} / \langle \Delta y \rangle \right)$ is the minimum buffer size in

704   JSG pixels; choice of using $+$ or $-$ depends on which side of D the Sun is on. For EarthCARE,

705     $d_{\perp}^{\min} = 5$ km. One then determines the highest cloud in the row of JSG pixels at distance j pixels

706   from L2-plane as

707
$$h_{\parallel}(n,j) = \max\left\{h(i,j)\right\} : i \in \left[n - n_{buffer}^{\nwarrow}(n), n + n_{assess} + n_{buffer}^{\searrow}(n)\right].$$ (24)

708 If it happens that

709
$$h_{\parallel}(n,j) \geq \frac{abs(j - m_{assess})\langle \Delta y \rangle}{\tan\theta_0 \sin\varphi_r},$$ (25)

710 is satisfied at j, the across-track buffer gets reset to $m_{buffer} \leftarrow abs(j - m_{assess})$. This process is con-

711 tinued out to the edge of the MSI's swath. *Figure 5* is a schematic of this procedure. The aggrega-

712 tion of an assessment domain D and its buffer-zones is denoted as D^+.

713

References

Barker, H. W. and Z. Li, 1997: Interpreting shortwave albedo-transmittance plots: True or apparent anomalous absorption? *Geophys. Res. Let*., **24**, 2023-2026.

——, M. P. Jerg, T. Wehr, S. Kato, D. Donovan, and R. Hogan, 2011: A 3D Cloud Construction Algorithm for the EarthCARE satellite mission. *Q, J. R. Meteorol. Soc*., **137**, 1042–1058 DOI:10.1002/qj.824

——, S. Kato, and T. Wehr, 2012: Computation of Solar Radiative Fluxes by 1D and 3D Methods using Cloudy Atmospheres Inferred from A-train Satellite Data. *Surveys in Geophys*. **33**, 657-676.

——, J. N. S. Cole, and M. Shephard, 2014: Estimation of Errors associated with the EarthCARE 3D Scene Construction Algorithm. *Q. J. R. Meteorol. Soc.*, **140**, 2260–2271, DOI:10.1002/qj.2294.

——,——, C. Domenech, M. Shephard, C. Sioris, F. Tornow, and T. Wehr, 2015: Assessing the Quality of Active-Passive Satellite Retrievals using Broadband Radiances. *Q. J. R. Meteorol. Soc*., **141**, 1294–1305, DOI:10.1002/qj.2438.

——, P. M. Gabriel, Z. Qu, and S. Kato, 2021: Representativity of Cloud-Profiling Radar Observations for Data Assimilation in Numerical Weather Prediction. *Q. J. R. Meteorol. Soc.*, **147**, 1801–1822. https://doi.org/10.1002/qj.3996.

——, J. N. S. Cole, Z. Qu, N. Villefranque, and M. W. Shephard, 2023: Radiative Closure Assessment of Retrieved Cloud and Aerosol Properties for the EarthCARE Mission: The ACMB-DF Product. *Atmos. Meas. Tech.*, to be submitted.

Cole, J. N. S, H. W. Barker, Z. Qu, N. Villefranque, and M. W. Shephard, 2023: Broadband Radiative Quantities for the EarthCARE Mission: The ACM-COM and ACM-RT Products. *Atmos. Meas. Tech.*, to be submitted.

Donovan, D. P., P. Kollias, and G-J van Zadelhoff, 2023: The Generation of EarthCARE L1 Test Data sets Using Atmospheric Model Data Sets. *Atmos. Meas. Tech.*, to be submitted

Eisinger, M., T. Wehr, T., Kubota, D., Bernaerts, and K. Wallace, 2023: The EarthCARE production model and auxiliary products. *Atmospheric Measurement Techniques*, to be submitted.

ESA., 2001: *The Five Candidate Earth Explorer Missions: EarthCARE –Earth Clouds, Aerosols and Radiation Explorer,* ESA SP-1257(1), September 2001. ESA Publications Division: Noordwijk, The Netherlands.

Illingworth, A. + others, 2015: THE EARTHCARE SATELLITE: The next step forward in global measurements of clouds, aerosols, precipitation and radiation. *Bull. Am. Met. Soc*., **96**, 1311-1332. DOI:10.1175/BAMS-D-12-00227.1.

—— + others, 2018: WIVERN: A New Satellite Concept to Provide Global In-Cloud Winds, Precipitation, and Cloud Properties. *Bull. Am. Met. Soc*., **99**, 1669–1687. https://doi.org/10.1175/BAMS-D-16-0047.1

748 Marshak, A., A. Davis, W. Wiscombe, W. Ridgeway, R. Cahalan, 1998: Biases in Shortwave Column Ab-
749   sorption in the Presence of Fractal Clouds. *J. Climate*, **11**, 431-446.

750 Platnick, S., Ackerman, S., King, M., et al., 2015: MODIS Atmosphere L2 Cloud Product (06_L2). NASA
751   MODIS   Adaptive   Processing   System,   Goddard   Space   Flight   Center,   USA:
752   http://dx.doi.org/10.5067/MODIS/MOD06_L2.006.

753 Qu, Z., D. P. Donovan, H. W. Barker, Cole, J. N. S, M. W. Shephard, and V. Huijnen, 2023: Numerical
754   Model Generation of Test Frames for Pre-launch Studies of EarthCARE's Retrieval Algorithms and
755   Data Management System. *Atmos. Meas. Tech.*, to be submitted

756 Sun, X. J., H. R. Lia, H. W. Barker, R. W. Zhang, Y. B. Zhou and L. Liu, 2016:Estimation of cloud base
757   heights based on the matching of multiple cloud characteristics. *Q. J. R. Meteorol. Soc.*, **142**, 224-
758   232, DOI:10.1002/qj.2647.

759 Tornow, F., H. W. Barker, and C. Domenech, 2015: On the use of Simulated Photon Paths to Co-register
760   TOA radiances in EarthCARE Radiative Closure Experiments. *Q. J. R. Meteorol. Soc.*, **141**, 3239-
761   3251. DOI:10.1002/qj.2606.

762 USGS Earth Resources Observation and Science (EROS) Center, 2018: USGS EROS Archive - Land Cover
763   Products - Global Land Cover Characterization (GLCC) Background, https://www.usgs.gov/cen-
764   ters/eros/science/usgs-eros-archive-land-cover-products-global-land-cover-characterization-0#over-
765   view (last access: April 5, 2022).

766 van Zadelhoff, G.-J., H. W., Barker, E., Baudrez, S., Bley, N., Clerbaux, J. N. S., Cole, J., de Kloe, N.,
767   Docter, C., Domenech, D. P., Donovan, J.-L. Dufresne, M., Eisinger, J., Fischer, R., García-Marañón,
768   M., Haarig, R. J., Hogan, A., Hünerbein, P., Kollias, R., Koopman, T., Wehr, 2022: EarthCARE level-
769   2 demonstration products from simulated scenes (09.01) [Data set]. Zenodo.
770   https://doi.org/10.5281/zenodo.7117116

771 Velázquez-Blázquez, A., E. Baudrez, N., Clerbaux, C., Domenech, R. G., Marañón, and N. Madenach,
772   2023: Towards instantaneous top-of-atmosphere fluxes from EarthCARE: The BMA-FLX product.
773   *Atmospheric Measurement Techniques*, to be submitted.

774

775

Page 22: [1] Deleted   Howard   2/9/23 1:47:00 PM

Page 22: [1] Deleted   Howard   2/9/23 1:47:00 PM

Page 22: [1] Deleted   Howard   2/9/23 1:47:00 PM

Page 22: [2] Moved to page 21 (Move #7)   Howard   2/9/23 1:47:00 PM

Page 22: [2] Moved to page 21 (Move #7)   Howard   2/9/23 1:47:00 PM